

ARTICLE OPEN



Emergent ferromagnetism and insulator-metal transition in δ -doped ultrathin ruthenates

Zeeshan Ali¹, Mohammad Saghayezhian¹, Zhen Wang^{1,2,3}, Andrew O'Hara⁴, Donghan Shin⁴, Wenbo Ge⁵, Ying Ting Chan⁵, Yimei Zhu^{2,6}, Weida Wu⁵, Sokrates T. Pantelides^{4,6} and Jiandi Zhang^{1,7}

Heterostructures of complex transition metal oxides are known to induce extraordinary emergent quantum states that arise from broken symmetry and other discontinuities at interfaces. Here we report the emergence of unusual, thickness-dependent properties in ultrathin CaRuO₃ films by insertion of a single isovalent SrO layer (referred to as δ -doping). While bulk CaRuO₃ is metallic and nonmagnetic, films thinner than or equal to \sim 15-unit cells (u.c.) are insulating though still nonmagnetic. However, δ -doping to middle of such CaRuO₃ films induces an insulator-to-metal transition and unusual ferromagnetism with strong magnetoresistive behavior. Atomically resolved imaging and density-functional-theory calculations reveal that the whole δ -doped film preserves the bulk-CaRuO₃ orthorhombic structure, while appreciable structural and electronic changes are highly localized near the SrO layer. The results highlight delicate nature of magnetic instability in CaRuO₃ and subtle effects that can alter it, especially the role of A-site cation in electronic and magnetic structure additional to lattice distortion in ruthenates. It also provides a practical approach to engineer material systems via highly localized modifications in their structure and composition that may offer new routes to the design of oxide electronics.

npj Quantum Materials (2022)7:108; <https://doi.org/10.1038/s41535-022-00518-7>

INTRODUCTION

Complex-oxide heterostructures have been established as an effective engineering platform offering prospects to create tunable electro-magnetic functionalities, enabled by manipulation of the cooperative interplay between electronic spin, charge, orbital, and lattice degrees of freedom^{1,2}. The stacking of different oxides disturbs the subtle equilibrium among various interactions, leading to a wealth of exotic quantum states, such as two-dimensional electron or hole gas at the interface of two insulating materials such as LaAlO₃/SrTiO₃ (LAO/STO)^{3,4}, the spontaneous magnetic reversal in La_{2/3}Sr_{1/3}MnO₃ films⁵, a ferromagnetic (FM) interface between nonmagnetic constituents^{6,7}, polar magnetic metal phase in BaTiO₃/SrRuO₃/BaTiO₃ heterostructures⁸, chiral ferromagnetism in SrRuO₃ films⁹, and strain-induced superconductivity in RuO₂ films¹⁰. The continued advancements in thin-film synthesis have made possible the fabrication of complex-oxide layers down to extremely thin limits with atomic precision, providing fine control over different lattice structures and paving the pathway to observe unusual quantum states^{11–15}.

The two ABO₃ 4d-perovskite structure ruthenates CaRuO₃ (CRO) and SrRuO₃ (SRO), despite having similar structure and electron counting, present unusual contrast in their physical properties. SRO is a strong Stoner metallic ferromagnet^{16,17}; while CRO, though a metal¹⁷, lacks long-range magnetic order^{18,19}. Extensive experimental and theoretical studies led to lively debates on the origin of the contrasting behavior, though the most likely explanation is that the impact of replacing Sr with Ca in SRO is indirect. The smaller ionic radius of Ca (2.31 Å versus 2.55 Å for Sr) leads to different octahedral Ru–O–Ru bond angles that result in subtle changes of the Fermi-energy density of states (DOS)^{20–22}.

Thin films of CRO and SRO also exhibit distinct properties, depending on temperature, film thickness, substrate strain, and film stoichiometry. Relatively thick CRO films grown on STO (001) have been reported to be metallic²³, yet under similar epitaxial strain, an insulating CRO phase can emerge below a certain critical thickness^{24,25}, which depends on growth conditions and is much larger than the critical thickness (2–3 u.c.) for similar behavior by SRO films^{26,27}. At present, the intrinsic critical thickness of stoichiometric CRO films is not known. In addition, theoretical calculations predicted that tensile epitaxial strain can drive CRO to a FM state²⁸, yet experimental confirmation is lacking²⁹. Moreover, cation substitution at Ru sites by defects/dopants has also attracted considerable attentions as a way to induce FM order in CRO, suggesting an extremely fragile ground state^{30–35}. Therefore, the delicate nature of incipient ferromagnetism in CRO suggests that one can manipulate CRO thin films in unique ways to obtain unusual, even unexpected electro-magnetic properties.

The present work focuses on ultrathin CRO films, which we perturb by inserting a single SrO layer (thus, mimicking a single-u.c. of SRO^{14,15} or δ -doping^{36,37}) in the middle of the films, all fabricated with atomic precision. Combining magneto-transport measurements, atomically resolved imaging by scanning transmission electron microscopy (STEM), and electron energy-loss spectroscopy (EELS), along with density-functional-theory (DFT) calculations, we reveal a thickness-dependent metal to insulator transition (MIT) with no sign of long-range magnetic ordering in pristine CRO films. As the thickness reaches 15 or fewer u.c., the films become insulating. However, the insertion of a single SrO layer not only triggers an insulator-to-metal transition in the

¹Department of Physics & Astronomy, Louisiana State University, Baton Rouge, LA 70803, USA. ²Condensed Matter Physics & Materials Science, Department, Brookhaven National Laboratory, Upton, NY 11973, USA. ³University of Science and Technology of China, Hefei, Anhui 230026, People's Republic of China. ⁴Department of Physics and Astronomy, Vanderbilt University, Nashville, TN 37235, USA. ⁵Department of Physics and Astronomy, Rutgers University, Piscataway, NJ 08854, USA. ⁶Department of Electrical Computer Engineering, Vanderbilt University, Nashville, TN 37235, USA. ⁷Beijing National Laboratory for Condensed Matter Physics, Institute of Physics, Chinese Academy of Sciences, Beijing 100190, People's Republic of China. ✉email: zhu@bnl.gov; pantelides@vanderbilt.edu; jiandiz@iphy.ac.cn

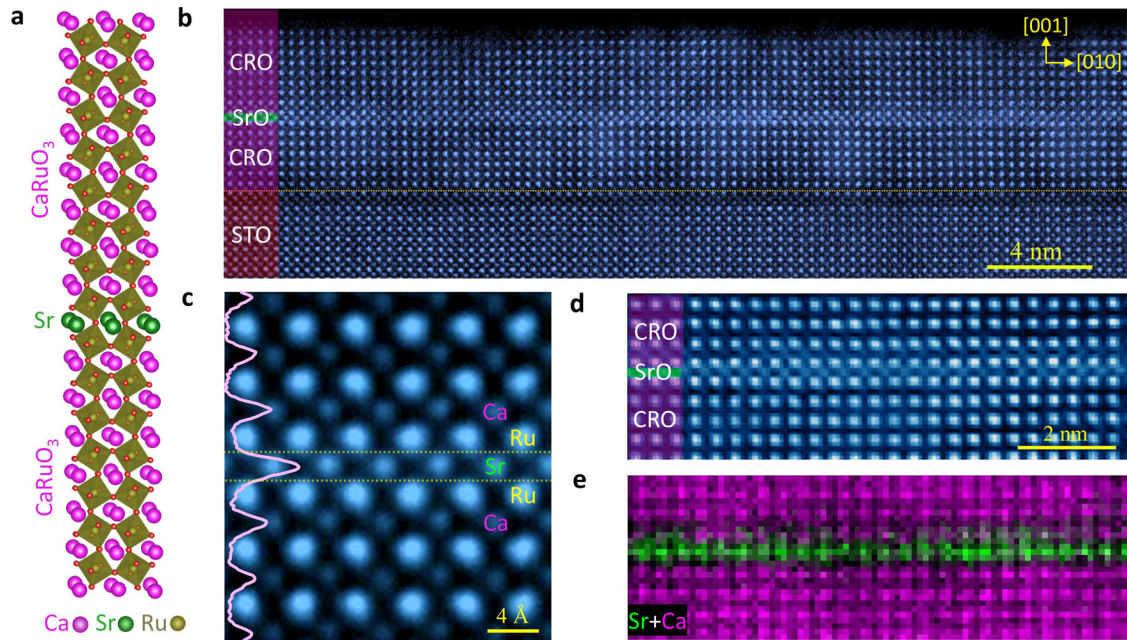


Fig. 1 Heterostructure design and atomic-scale visualization of $\text{CRO}^7\text{-SrO-CRO}^8$ heterostructure. **a** Schematic of the nested SrO δ -doping in CaRuO_3 . Atomic-resolution high-angle annular dark-field (HAADF) images of δ -doped $\text{CRO}^7\text{-SrO-CRO}^8$ heterostructure: **b** large-area HAADF image, and **c** highly magnified HAADF with superimposed intensity profiles of Ca/Sr layer. **d** Annular dark field (ADF) image and **e** corresponding electron energy loss spectroscopy (EELS) mapping for Ca (purple) and Sr (green) cations. The electron beam is along the $[100]$ direction of the STO substrate.

15 u.c. CRO films and enhances the conductivity of thicker films, but also drives the studied thin films (15–40 u.c.) toward emergent Griffiths-like phase and unusual ferromagnetism. Atomic-resolution imaging and DFT calculations reveal that SrO-layer insertion preserves the orthorhombic symmetry, and the structural and electronic changes are largely confined near the insertion layer. Our results underline the fragile nature of the magnetic properties and likely the electronic structure of CRO by which a highly localized modification is able to tip the delicate balance for both transport and magnetic ordering in the system.

RESULTS

Atomic-scale structure and composition

We have fabricated epitaxial 15-u.c. CRO (CRO^{15}), 20-u.c. CRO (CRO^{20}), and 40-u.c. CRO (CRO^{40}) films on SrTiO_3 (001) substrates, and corresponding δ -doped CRO films containing a localized SrO layer nested in the middle, i.e., $\text{CRO}^7\text{-SrO-CRO}^8$, $\text{CRO}^{10}\text{-SrO-CRO}^{10}$, and $\text{CRO}^{20}\text{-SrO-CRO}^{20}$. Figure 1a shows a schematic of the $\text{CRO}^7\text{-SrO-CRO}^8$ heterostructure while Fig. 1b–d displays the atomically resolved structure of the same system. Our X-ray diffraction data (see Supplementary Information Note 1), and STEM measurements demonstrate that these films are fully strained to the substrate with high crystallinity (see Supplementary Fig. 2). The STEM results confirm microscopically that the heterostructures have a homogeneous SrO layer and coherent interfaces. It is apparent from the STEM image that the $\text{CRO}^7\text{-SrO-CRO}^8$ heterostructure is uniform with coherent and high-quality hetero-interfaces (Fig. 1b–d and Supplementary Fig. 3). In Z-contrast High-angle annular dark-field (HAADF) images, Sr ($Z = 38$) columns appear brighter than Ca ($Z = 20$), whereby a uniform and homogeneous single Sr layer is observed clearly in Fig. 1c and Supplementary Figs. 3, 4. Furthermore, the electron energy loss spectroscopy (EELS) elemental maps of Ca (purple) and Sr (green) (Fig. 1e and Supplementary Fig. 4) confirm that Sr is confined within a single layer with minimal if any intermixing, establishing that the nested SrO is a monolayer.

The high-resolution STEM imaging permits us to reveal the structural distortions (see Fig. 2). The orthorhombic (CRO) unit-cell oriented on the cubic STO (001) grows in the $[110]_O$ direction. Consequently, either in-phase $[001]_O$ or out-of-phase $[1-10]_O$ rotation axis can align along the $[100]$ direction of STO; generating two different structural domains with a 90° rotation (referred as A and B, see Supplementary Note 3 for details)^{38,39}. Viewing along the $[100]$ direction of STO substrate, we can acquire projected structures of the film in the $[001]_O$ direction from domain A and the $[1-10]_O$ direction from domain B, simultaneously. In domain A, the in-phase octahedral rotation axis is along the STO $[100]$, hence allowing the visualization of RuO_6 octahedron tilt (Fig. 2a, c). In contrast, for domain B, the direct imaging of octahedral tilt is not possible, but orthorhombicity related A-site cation displacements can be measured as displayed in Fig. 2b, e. The projected octahedral tilt (θ as denoted in Fig. 2c, d) extracted from the ABF images of domain A (Fig. 2a, c) shows that except at the 1st unit-cell near film-substrate interface ($\theta \approx 8.4^\circ$), the RuO_6 tilt angle in the CRO film is constant ($\theta \approx 11^\circ$); a nearly identical behavior as that of CRO bulk ($\theta \approx 11.5^\circ$). Hence, the octahedral mismatch is adjusted close to the film-substrate interface, where TiO_6 interfacial layers on the STO side undergo significant distortion to accommodate the octahedral mismatch of $\text{RuO}_6\text{-TiO}_6$ (bulk CaRuO_3 : $\theta \approx 11.5^\circ$ versus SrTiO_3 : $\theta \approx 0^\circ$). Additionally, we note that the 15-u.c. undoped CRO film also has $\theta \approx 11^\circ$ (see Supplementary Note 4). Therefore, the octahedral network structure is not altered by the SrO-interlayer insertion. Instead, due to a corner-connectivity constraint, the octahedral geometry is conserved throughout the entire δ -doped heterostructure, i.e., the structure preserves bulk-CRO orthorhombic symmetry.

The A-site cation displacements (x_A), a signature of orthorhombicity^{37,40} were determined quantitatively for individual layers with the domain B imaging (Fig. 2b, e as well as Supplementary Figs. 5–8). It is seen that the δ -doped heterostructure (see Fig. 2f) shows an averaged Ca-site $x_A \approx 0.38 \pm 0.07 \text{ \AA}$, which matches that of a pristine CRO film ($x_A \approx 0.38 \pm 0.07 \text{ \AA}$, see Supplementary Fig. 8), while slightly smaller than CRO bulk ($x_A \approx 0.43 \text{ \AA}$, see Fig. 2g).

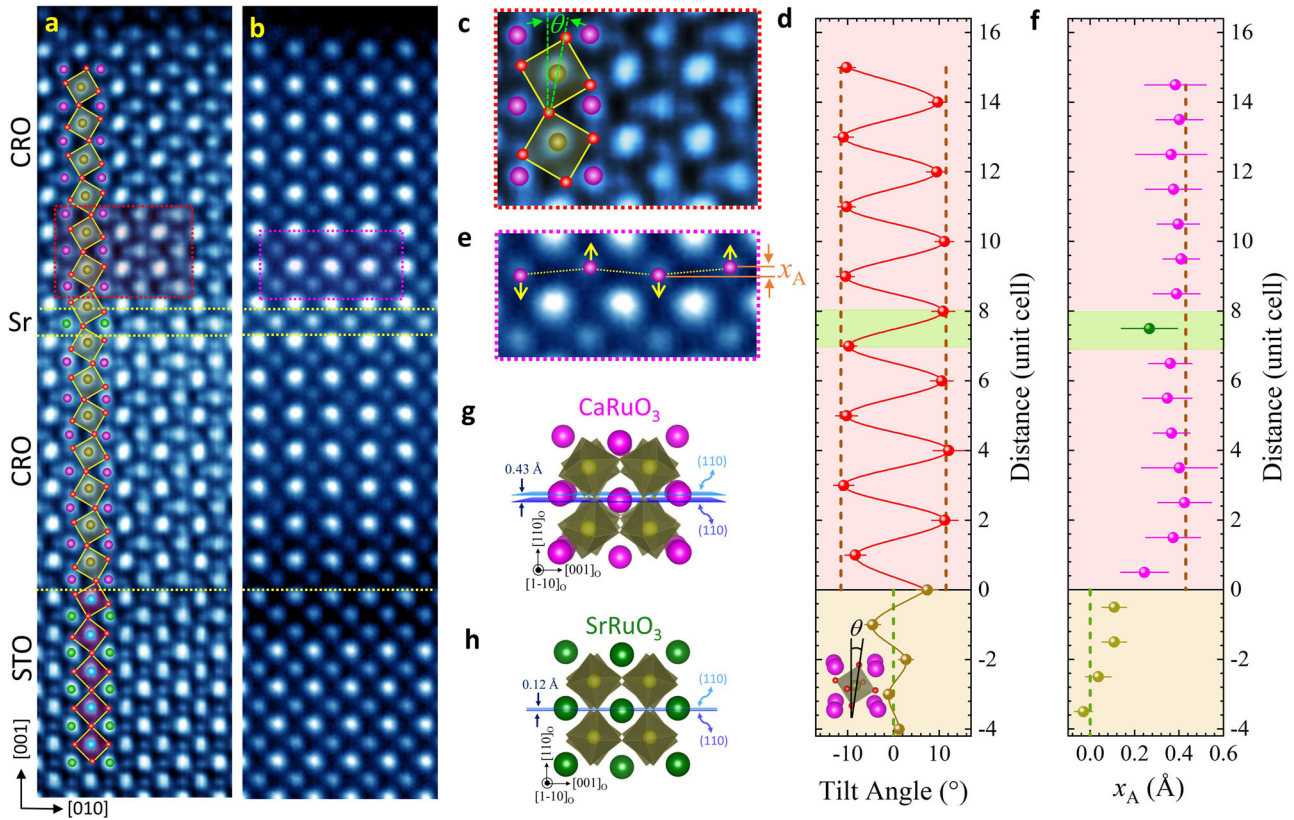


Fig. 2 Atomically resolved structure of $\text{CRO}^7\text{-SrO-CRO}^8$ heterostructure. **a** intensity-inversed annular bright field (ABF), and **b** High-angle annular dark-field (HAADF) images representing domain A and B, respectively. **c** Zoom-in image of the area marked in **a** superimposed by projected octahedra and tilt angle (θ), and **d** θ as a function of distance from the film-substrate interface. **e** Zoom-in image of the area marked in **b** superimposed by the corresponding A-site cation displacement (x_A), and **f** x_A versus atomic distance. The arrows in **e** mark the A-site displacement direction thus forming an up-down buckling pattern in AO plane. The dashed lines in **d** and **f** represent the value of θ and x_A of bulk CRO (brown) and STO (green), respectively. Schematic of the bulk crystal structure of **g** CRO and **h** SRO showing A-site displacement projected along $[1-10]_o$ direction. The top (110) plane (light blue) passes through the center of the left and right Ca (Sr) atom, and the dark blue (110) plane bisects the center of the middle Ca (Sr)-atom, whereas the projected A-site displacement corresponds to the distance between the two parallel planes. The error bar in panels **d** and **f** indicates the standard deviation of averaged measurement for each vertical atomic column.

On the other hand, the x_A at nested SrO is reduced to $0.26 \pm 0.10 \text{ \AA}$ (see Fig. 2f), but it is significantly larger than that in bulk SrRuO_3 ($x_A \approx 0.12 \text{ \AA}$, see Fig. 2h). These observations suggest a small local structural modification is present in the SrO layer, which is induced by the ionic (Ca/Sr) radius mismatch.

Electron transport of pristine and δ -doped CaRuO_3 films

To understand the δ -doping effect on the electronic properties of CRO films, we have systematically measured the transport behavior of the CRO films with and without SrO insertion. Figure 3a shows the sheet resistance temperature evolution of pristine and δ -doped CRO films for different thicknesses. As shown in Fig. 3a, the thicker pristine CRO^{40} film exhibits bulk-like metallic transport ($d\rho/dT > 0$) down to $\sim 21 \text{ K}$, followed by a small resistivity upturn (see Supplementary Fig. 9 for details), characterized by weak localization^{41–45}. The intermediate thickness CRO^{20} film features a metallic behavior at high temperatures, but exhibits a resistivity upturn below $\sim 95 \text{ K}$. Such a robust resistivity upturn at low temperatures is frequently observed in many metallic oxide films, especially close to the verge of a metal–insulator transition^{41–44}. Finally, the 15 u.c. (CRO^{15}) film is identified to be fully insulating ($d\rho/dT < 0$ at all temperatures), where $\rho(T)$ exhibits variable range hopping (VRH) (see Fig. 3b, c and Supplementary Note 5 for more details). Specifically, the CRO^{15} transport follows a Mott-type VRH [$\ln(\rho) \propto T^{-1/3}$] above $\sim 25 \text{ K}$ (see Fig. 3b), indicating that the transport is

governed by disorder-driven Anderson localization^{46–48}. At low temperatures, a crossover to Efros-type VRH [$\ln(\rho) \propto T^{-1/2}$] is observed (Fig. 3c), likely suggesting the significance of electron–electron interactions in the strong localization regime^{49–52}. In contrast to insulating CRO^{15} , the δ -doped film i.e., $\text{CRO}^7\text{-SrO-CRO}^8$ displays improved conductivity holding a room temperature metallicity, though a strong upturn appears below $\sim 250 \text{ K}$ (see the inset of Fig. 3a). Likewise, the δ -doping consistently lowers the resistivity and resistivity upturn temperatures, as seen in $\text{CRO}^{10}\text{-SrO-CRO}^{10}$ and $\text{CRO}^{20}\text{-SrO-CRO}^{20}$ (see Fig. 3a).

The δ -doping of CRO films not only triggers the enhancement of conductivity but also induces a pronounced ferromagnetic order revealed by magnetoresistance: $\text{MR} = \{\rho(H) - \rho(0)\} / \rho(0)$, where $\rho(H)$ and $\rho(0)$ are resistivities with and without magnetic field, respectively. The MR in pristine CRO^{40} and CRO^{20} is very small, as expected for paramagnetic metallic systems (Fig. 3d). However, the MR is monotonically enhanced with reducing film thickness to CRO^{15} due to the charge localization. At the same time, a very small, but noticeable MR hysteresis could be observed in CRO^{15} , signifying a weak and possibly short-range ferromagnetic fluctuation phase^{53,54}. Meanwhile, the low-field MR in CRO^{15} is positive (see blue arrows in Fig. 3d) and becomes negative at higher fields. The positive MR is a sign of electron–electron correlations (EEC) that are robust at low temperatures, consistent with the presence of Efros-type VRH $\rho(T)$ behavior (see Fig. 3c)^{55–57}. In contrast, as shown in Fig. 3e, the δ -doping in CRO^{15}

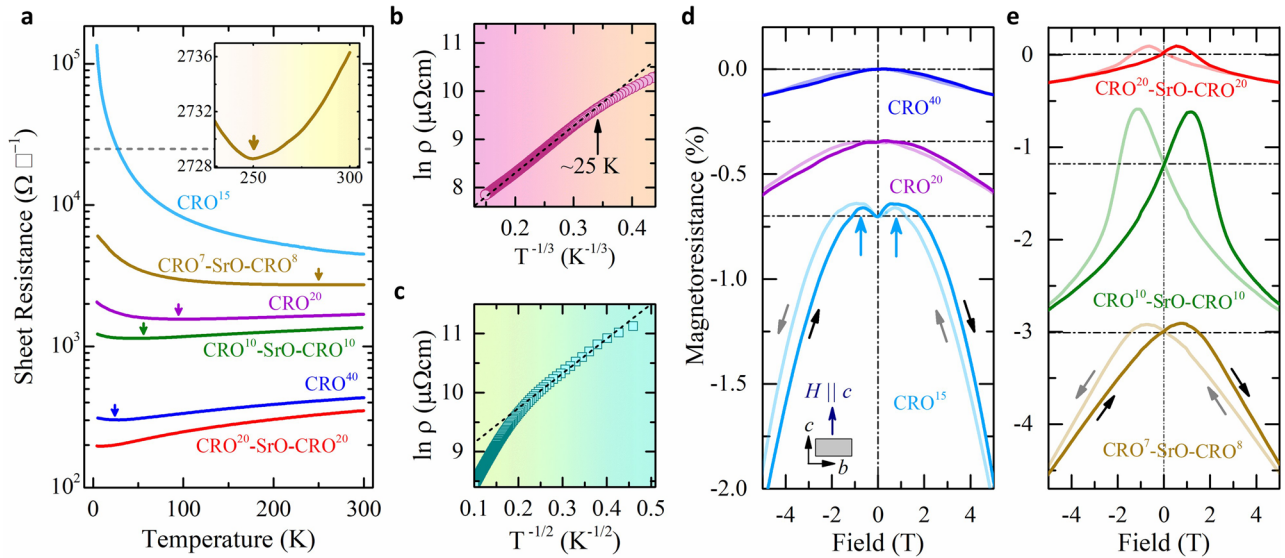


Fig. 3 Electron transport of pristine and δ -doped CRO films. **a** Temperature-dependent sheet resistance. In panel **a** the dashed gray-line marks the Mott–Ioffe–Regel limit representing quantum of resistance ($h/e^2 \approx 25 \text{ k}\Omega/\square$), while the arrows indicate the characteristic temperature below which a resistivity upturn occurs. The inset of **a** shows the temperature-dependent sheet resistance of $\text{CRO}^7\text{-SrO-CRO}^8$, highlighting the resistivity upturn. Logarithmic plots of CRO^{15} resistivity as a function of **b** $T^{-1/3}$ (Mott VRH), and **c** $T^{-1/2}$ (Efros VRH). **d, e** Magnetoresistance (MR) at $T = 5 \text{ K}$ with the magnetic field applied along the film normal. The MR curves in **d, e** are offset to prevent overlapping.

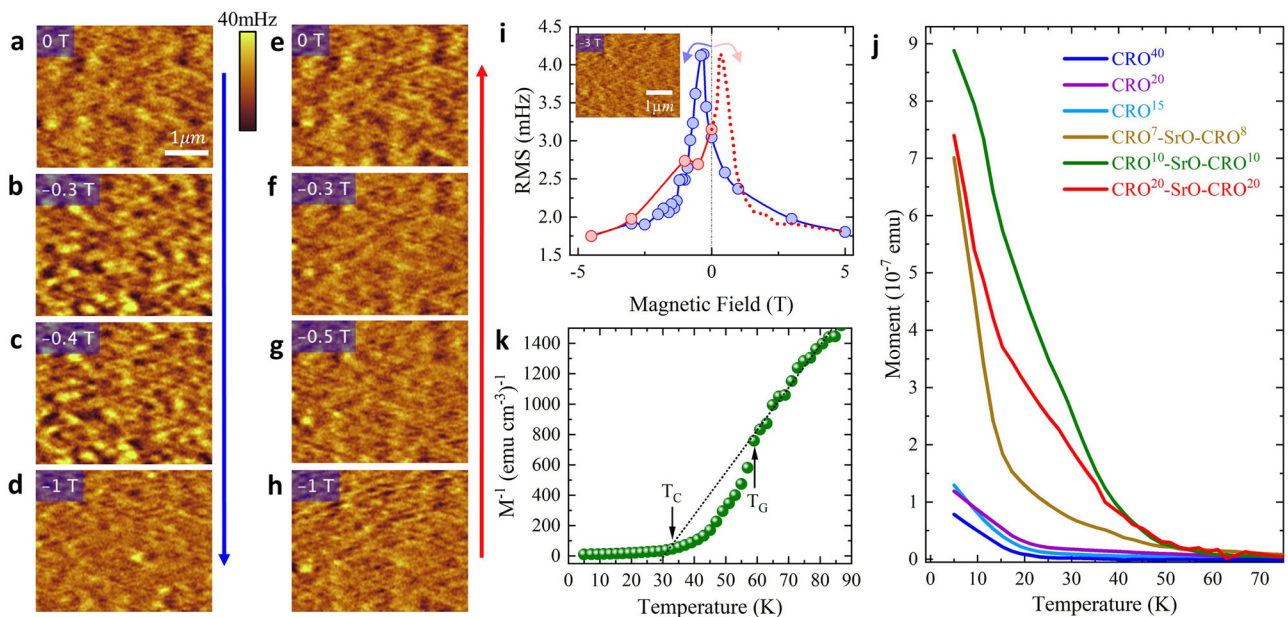


Fig. 4 Magnetic force microscopy (MFM) images of the δ -doped $\text{CRO}^{10}\text{-SrO-CRO}^{10}$ heterostructure. The MFM images are taken in the increasing **a–d** and decreasing field **e–h** process (indicated by arrows). **i** Field-dependent root-mean-square (RMS) data. The inset in **i** is the MFM image of the same area measured at -3 T displaying a typical saturated state. **j** Temperature-dependent magnetization of different thickness of undoped and δ -doped CRO films. **k** $\text{CRO}^{10}\text{-SrO-CRO}^{10}$ magnetization (M) inverse as a function of temperature. The black dotted line in **k** indicates a guide for the linear fit.

(i.e., $\text{CRO}^7\text{-SrO-CRO}^8$) leads to a clear butterfly-like hysteretic MR, representative of ferromagnetic order^{14,15,58–61}. In parallel to this, the positive MR detected in pristine CRO^{15} is also diminished (see Fig. 3d, e), supporting the conjecture that the emergence of ferromagnetic ordering involves modification of electronic correlations^{35,62}. In addition, as shown in Fig. 3e, a distinctive FM-induced hysteretic MR is also spotted in both $\text{CRO}^{10}\text{-SrO-CRO}^{10}$ and $\text{CRO}^{20}\text{-SrO-CRO}^{20}$ heterostructures, validating the appearance of FM order induced via benign δ -doping of CRO.

Magnetic characterization

To further reveal the unusual magnetic behavior in the δ -doped films, we performed cryogenic magnetic force microscopy (MFM) studies (see Supplementary Note 6 for more details). The MFM images of the $\text{CRO}^{10}\text{-SrO-CRO}^{10}$ in different magnetic fields at 5.5 K are shown in Fig. 4a–h. There is weak bubble-like magnetic contrast (bright-dark pattern) in the zero-field MFM image after the sample was saturated at a positive field (6 T), indicating magnetic inhomogeneity. The magnetic contrast is barely above

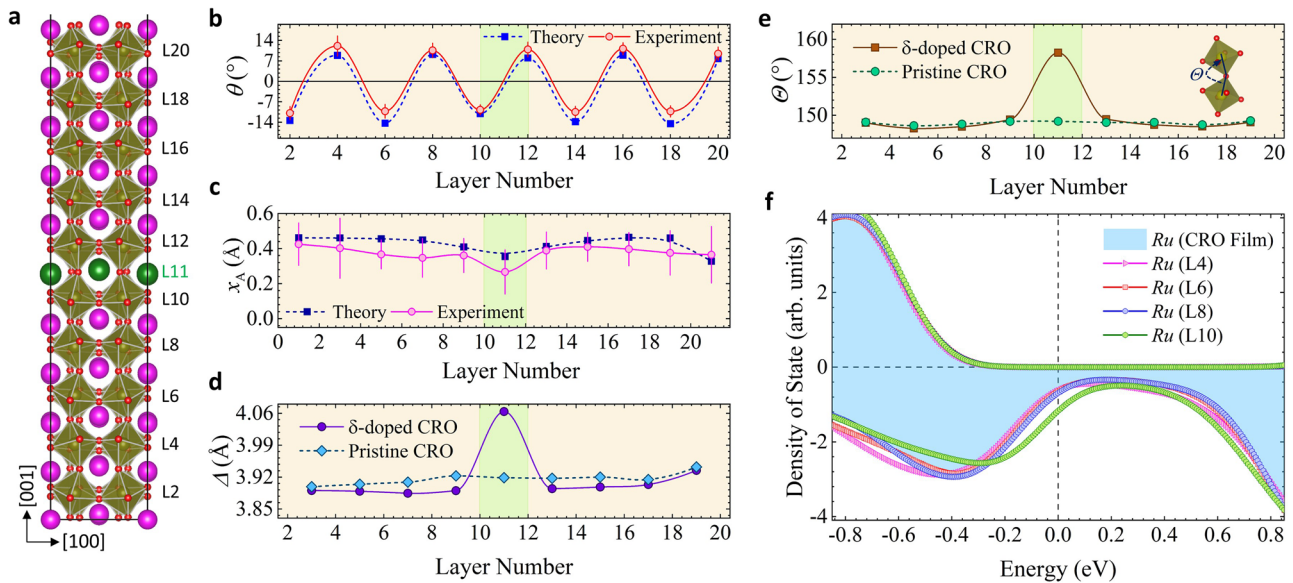


Fig. 5 Density functional theory calculations of δ -doped heterostructure. **a** Schematic representation of δ -doped heterostructures, where one of the Ca atomic (purple) layers is replaced by Sr atoms (green). **b** Theoretical and experimental projected octahedral tilt angle (θ), and **c** A-site cation displacement (x_A). The experimental error-bar in panels **b**, **c** is standard deviation of averaged measurement. **d** Calculated RuO_2 interlayer spacing (Δ), and **e** three-dimensional octahedron bond angle (Θ). **f** Layer-by-layer Ru-projected DOS of the heterostructure, with the selected layers labeled as in panel **a**. Up-spins (majority) are represented as positive and down spins (minority) as negative.

the noise level of our MFM system. These features suggest that the FM order in the ground state is not fully long-range. With an increasing magnetic field, the dark-bright contrast increases strongly. More bubble-like magnetic contrast emerges at -0.3 to -0.4 T (see Fig. 4b, c), indicating inhomogeneous switching of magnetic order. The field dependence of the magnetic contrast as measured by the root-mean-square (RMS) value of the MFM images (Fig. 4i) shows a sharp peak between 0 T and -1 T. While reaching its maximum value at around -0.3 T, the magnetic contrast is barely visible below -1 T, indicating that the sample is approaching saturation (see Fig. 4d). In accord with the above, the RMS value varies very little below -1 T. A typical MFM image of the sample at saturation is shown by the inset of Fig. 4i. In contrast to the negative ramping, relatively uniform magnetic contrast was observed between -6 and 0 T after saturating the sample at -6 T as in Fig. 4h–e. Consistently, the RMS values of the MFM images do not vary much as shown in Fig. 4i, demonstrating the hysteretic behavior of the magnetic order. Overall, the evolution of the magnetic contrast and their hysteretic behavior provide supporting evidence of unusual ferromagnetism without fully long-range ordering in the sample.

The magnetization as a function of temperature [$M(T)$] for pristine and δ -doped CRO films is shown in Fig. 4j. All pristine CRO films show a paramagnetic-like signal reminiscent of the STO substrate with no clear signs of a ferromagnetic transition. On other hand, SrO δ -doping in the middle of the CRO films induces a FM order since the $M(T)$ represents a paramagnetic to ferromagnetic transition. However, the $M(T)$ curves in the δ -doped CRO films have a rather unusual T -dependence. At low temperature, they show a non-typical long-range order $M(T)$ line shape with a very weak upturn between 35 and 60 K. Above this temperature range, the magnitude of magnetization increases, but is still relatively weak compared to its sister counterpart, SrRuO_3 films⁶³. The presence of ferromagnetism is further corroborated by an anomalous Hall effect (see Supplementary Fig. 13 for details).

Normally, a long-range ordered FM system above T_C obeys Curie–Weiss (CW) law; $\chi = \frac{C}{T - \theta_{\text{CW}}} = \frac{M}{H} \Rightarrow M^{-1} \propto (T - \theta_{\text{CW}})$, where C is the CW constant and θ_{CW} is the Weiss temperature, so that M^{-1} is linearly proportional to T above T_C . In our case here, a

measurement of χ is not feasible due to the extremely thin films, but the T -dependent inverse of magnetization [$M^{-1}(T)$] can shed light on the unusual CW behavior. As shown in Fig. 4k, the $M^{-1}(T)$ of $\text{CRO}^{10}\text{-SrO-CRO}^{10}$ in the paramagnetic state exhibits decent linearity only above a characteristic temperature $T_G \approx 60$ K, but a sudden downturn occurs below T_G . Such a deviation from the CW law in the temperature range $T_C < T < T_G$ is reminiscent of a Griffiths-phase (GP) phenomenon (T_G is referred to as Griffith's temperature)^{19,64–67}. The GP is characterized by the coexistence of ferromagnetic entities within the globally paramagnetic phase, causing a non-analytical behavior in magnetic susceptibility with characteristic departure from Curie–Weiss behavior in the vicinity of T_C and T_G . Such a GP signature has been reported in bulk Ca-doped SrRuO_3 , where Ca substitution for Sr introduces ferromagnetic spin–spin coupling dilution through Ru–O–Ru bonds, and leads to T_C reduction¹⁹.

Density functional theory (DFT) calculations

We have performed DFT calculations on the heterostructure shown schematically in Fig. 5a to gain additional insights into the observed phenomena (see Supplementary Note 8 for details). Analyzing the structural changes due to the δ -doping, we find that the plane-projected octahedral tilt angle θ (Fig. 5b) remains essentially unchanged, whereas in Fig. 5c, a dip in the A-site cation displacement (x_A) is consistent with the STEM data of Fig. 2. Additionally, by looking at the RuO_2 interlayer spacing (Δ), a significant increase at the place of the δ -layer site occurs paralleling the dip in x_A (Fig. 5d). Although not evident in the projected tilt angle (θ) measured by STEM, there is a large change in the 3D octahedral angle (defined as Θ , see Fig. 5e) at the δ -doping layer. Taken together, these results indicate that the insertion of the δ -doping layer causes a highly local modification of the atomic structure confined between the adjacent RuO_2 layers.

In Fig. 5f, we show the calculated Ru-projected density of states (DOS) for the pristine CRO thin-film in the layers adjacent to the CaO layer that gets replaced by SrO (blue-shaded region). It is clear that the thin-film is semi-metallic^{8,22}. We assume that such a thin film models CRO^{15} , which according to Fig. 3d, is on the verge

of being ferromagnetic (the accuracy of our DFT + U calculations would not allow us to reliably predict at what thickness such a state would exist). In Fig. 5f, we also show the Ru-projected DOS for the δ -doped film in several layers near the SrO plane (see also Supplementary Fig. 15). We note that the DOS in the immediately adjacent (green curves) differs from the others in that it signifies an enhancement of the DOS at the Fermi energy by approximately a factor of 2.

DISCUSSION

If some form of disorder is present at increasing levels as the film thickness is reduced, the thinnest film may have sufficient disorder to induce Anderson localization in the small number of states at the Fermi energy E_F throughout the CRO film. Hence a MIT occurs at a critical thickness. If we then assume that the same level of disorder is present in a doped film as in an undoped film we reason as follows. In films of all thicknesses, a doped film has a larger DOS at E_F in the vicinity of the SrO layer than in the corresponding undoped film. Thus, in all doped films, only a fraction of the propagating states in the region of the SrO layer undergo localization, creating a mobility edge, i.e., propagating states remain so, and the MIT is avoided. This effect enhances the conductivity of films above the critical thickness, as observed. For thin films below the critical thickness, the same effect induces metallic behavior in the region of the SrO layer, which is also in agreement with the experimental data since the data cannot tell if the film is conducting throughout or only in the region of the SrO layer. As for the Griffiths-phase-like ferromagnetism in doped CRO films, the above analysis also tells us that there may be sufficient density of propagating states at E_F in the SrO region to satisfy the Stoner criterion locally. We can then speculate that nonlocal exchange may trigger a domino effect, which generates patchy ferromagnetism throughout the CRO film. It is not currently practical to perform DFT calculations in large heterostructures using hybrid functionals that include nonlocal exchange and check if the formation of FM patches in the CRO film lowers the total energy. The domino possibility remains to be tested.

In summary, we show that CaRuO_3 , otherwise being metallic and at the verge of a magnetic critical point, retains its nonmagnetic nature but becomes insulating in thin film form under a critical thickness (15 u.c.). In contrast, δ -doping a single layer of SrO into ultra-thin CRO films results in an unusual ferromagnetism and a transition back to a metallic state while the entire heterostructures preserve the bulk-CRO orthorhombic lattice symmetry. Atomic-resolution imaging along with DFT calculations find that SrO-layer insertion causes highly local structural and electronic changes. The calculated DOS at the Fermi energy shows a noticeable enhancement near the insertion layer, leading to the probable local satisfaction of the Stoner criterion, which in turn may induce patchy ferromagnetism in the entire film by nonlocal exchange interactions. The observations demonstrate the fragility of the emerging magnetic state in CRO, shedding light on the role of A-site cation in electronic and magnetic structure additional to lattice distortion in ruthenates. These findings provide an innovative pathway to understanding the correlated system's electronic and magnetic nature through heterostructure architecture.

METHODS

Film growth, X-ray diffraction, and magneto-transport measurements

Pristine and δ -doped CaRuO_3 (CRO) films were grown on SrTiO_3 (001) substrates by pulsed laser deposition (PLD) at 700 °C with an oxygen pressure of 100 mTorr. The δ -doping of SrO was achieved from SrRuO_3 (SRO) target at a growth temperature of 700 °C and

oxygen pressure of 100 mTorr. The utilization of an SrRuO_3 target ensures the formation of the desired SrO-RuO₂ stacking formation. A KrF excimer laser ($\lambda = 248$ nm) with a 10 Hz repetition rate and laser energy density $\sim 1 \text{ J cm}^{-2}$ was used. After growth, samples were cooled down at $\sim 11^\circ/\text{min}$ to room temperature in an oxygen atmosphere of 100 mTorr. To monitor the film growth and thickness, the in-situ Reflection high-energy electron diffraction (RHEED) was employed. X-ray diffraction was performed on a Panalytical X'Pert thin-film diffractometer with $\text{Cu K}\alpha-1$ radiation with a single-crystal monochromator. The electron transport measurements were performed in a four-probe configuration on Quantum Design Physical Property measurement system (PPMS) in the temperature range of 5–300 K. For the magnetoresistance (MR), the external magnetic field was applied along the film normal. The magnetization was studied by using Quantum design SQUID (superconducting quantum interference device) reciprocating sample option (RSO). For magnetization as a function of temperature $M(T)$ measurements, the samples were first cooled down to 5 K under the 5000 Oe field, and then the data was acquired while warming in presence of 100 Oe field. The data points were smoothed using Locally Weighted Scatterplot Smoothing.

Scanning transmission electron microscopy (STEM) and electron energy loss spectroscopy (EELS)

The STEM and EELS results were attained using the 200 kV JEOL ARM electron microscope at Brookhaven National Laboratory (BNL) equipped with double aberration correctors, a dual energy-loss spectrometer, and a cold field emission source. Cross-sectional TEM samples were thinned using a focused ion beam with Ga^+ ions followed by Ar^+ ions milling down to sample thickness of 30 nm. The atomic-resolved STEM images were collected with a 21 mrad convergent angle (30 μm condenser aperture) and a collection angle of 67–275 mrad for HAADF and 11–23 mrad for ABF imaging. The STEM imaging conditions were optimized for simultaneous EELS acquisition with a probe size of 0.8 Å, a convergence semi-angle of 20 mrad, and a collection semi-angle of 88 mrad. EELS spectroscopy images were obtained across the whole film with a step size of 0.2 Å and a dwell time of 0.05 s/pixel. EELS spectra for composition distribution as well as Ru-L and Sr-L edges were acquired with energy dispersion of 1 eV/channel. The EELS spectra background was subtracted using a power-law function, and multiple scattering was removed by a Fourier deconvolution method.

Magnetic force microscopy (MFM)

The MFM experiments were carried out in a homemade cryogenic magnetic force microscope using commercial piezoresistive cantilevers (spring constant $\approx 3 \text{ N/m}$, resonant frequency $\approx 42 \text{ kHz}$)⁶⁸. The homemade MFM is interfaced with a Nanonis SPM controller and a commercial phase-lock loop (SPECS). The out-of-plane magnetic field was applied via a superconducting magnet. MFM tips were prepared by depositing a nominally 100 nm Co film onto the bare tips using sputtering. The MFM signal, the change of cantilever resonant frequency, is proportional to the out-of-plane stray field gradient. The sample surface is coated with Pt (15 nm)/Al (2 nm) bilayer to screen the electrostatic interaction.

Density-functional calculations

DFT calculations were performed using the Vienna ab initio Simulation Package (VASP)⁶⁹. The projector-augmented wave (PAW) method was used to describe the core-valence electron interactions^{70,71}. For bulk-like unit cells, a plane-wave basis cutoff energy of 600 eV was used and reduced to 450 eV for the heterostructure. The Perdew-Burke-Ernzerhof form of the generalized gradient approximation was employed for the exchange-correlation functional with a Hubbard U (see Supplemental

Information Note 8)^{72,73}. For bulk unit cells, the k-point sampling was performed using 8×8×8 Γ -centered grids. For the heterostructure, a 4×4×1 Γ -centered grid was used. The heterostructure considered was terminated with CaO on both sides and consists of 5-layers of CaO on each side of the SrO layer. RuO₂ layers have 4 Ru atoms/layer. A vacuum spacing of 15 Å along the z-axis was used to prevent spurious interactions between slabs due to periodic boundary conditions. In all cases, structures were relaxed until atomic forces were converged to be less than 0.02 eV/Å.

DATA AVAILABILITY

The data used in the study are available in the manuscript and supplementary data. The data that support the findings of this study are available from the corresponding author upon reasonable request.

Received: 6 June 2022; Accepted: 27 October 2022;

Published online: 10 November 2022

REFERENCES

- Hwang, H. Y. et al. Emergent phenomena at oxide interfaces. *Nat. Mater.* **11**, 103–113 (2012).
- Zubko, P., Gariglio, S., Gabay, M., Ghosez, P. & Triscone, J.-M. Interface physics in complex oxide heterostructures. *Annu. Rev. Condens. Matter Phys.* **2**, 141–165 (2011).
- Ohtomo, A. & Hwang, H. Y. A high-mobility electron gas at the LaAlO₃/SrTiO₃ heterointerface. *Nature* **427**, 423–426 (2004).
- Lee, H. et al. Direct observation of a two-dimensional hole gas at oxide interfaces. *Nat. Mater.* **17**, 231–236 (2018).
- Saghayezhian, M. et al. Atomic-scale determination of spontaneous magnetic reversal in oxide heterostructures. *Proc. Natl Acad. Sci. USA* **116**, 10309–10316 (2019).
- Brinkman, A. et al. Magnetic effects at the interface between non-magnetic oxides. *Nat. Mater.* **6**, 493–496 (2007).
- Takahashi, K. S., Kawasaki, M. & Tokura, Y. Interface ferromagnetism in oxide superlattices of CaMnO₃/CaRuO₃. *Appl. Phys. Lett.* **79**, 1324–1326 (2001).
- Meng, M. et al. Interface-induced magnetic polar metal phase in complex oxides. *Nat. Commun.* **10**, 5248 (2019).
- Wang, W. et al. Spin chirality fluctuation in two-dimensional ferromagnets with perpendicular magnetic anisotropy. *Nat. Mater.* **18**, 1054–1059 (2019).
- Ruf, J. P. et al. Strain-stabilized superconductivity. *Nat. Commun.* **12**, 59 (2021).
- Guo, H. et al. Interface-induced multiferroism by design in complex oxide superlattices. *Proc. Natl Acad. Sci. USA* **114**, E5062–E5069 (2017).
- Takiguchi, K. et al. Quantum transport evidence of Weyl fermions in an epitaxial ferromagnetic oxide. *Nat. Commun.* **11**, 4969 (2020).
- Sohn, B. et al. Observation of metallic electronic structure in a single-atomic-layer oxide. *Nat. Commun.* **12**, 6171 (2021).
- Ali, Z. et al. Origin of insulating and non-ferromagnetic SrRuO₃ monolayers. *Phys. Rev. B* **105**, 054429 (2022).
- Boschker, H. et al. Ferromagnetism and conductivity in atomically thin SrRuO₃. *Phys. Rev. X* **9**, 011027 (2019).
- Callaghan, A., Moeller, C. W. & Ward, R. Magnetic interactions in ternary ruthenium oxides. *Inorg. Chem.* **5**, 1572–1576 (1966).
- Bouchard, R. J. & Gillson, J. L. Electrical properties of CaRuO₃ and SrRuO₃ single crystals. *Mater. Res. Bull.* **7**, 873–878 (1972).
- Nguyen, L. T., Abeykoon, M., Tao, J., Lapidus, S. & Cava, R. J. Long-range and local crystal structures of the Sr_{1-x}Ca_xRuO₃ perovskites. *Phys. Rev. Mater.* **4**, 034407 (2020).
- Jin, C. Q. et al. High-pressure synthesis of the cubic perovskite BaRuO₃ and evolution of ferromagnetism in ARuO₃ (A = Ca, Sr, Ba) ruthenates. *Proc. Natl Acad. Sci. USA* **105**, 7115–7119 (2008).
- Mazin, I. I. & Singh, D. J. Electronic structure and magnetism in Ru-based perovskites. *Phys. Rev. B* **56**, 2556–2571 (1997).
- Maiti, K. Role of covalency in the ground-state properties of perovskite ruthenates: A first-principles study using local spin density approximations. *Phys. Rev. B* **73**, 235110 (2006).
- Rondinelli, J. M., Caffrey, N. M., Sanvito, S. & Spaldin, N. A. Electronic properties of bulk and thin film SrRuO₃: Search for the metal-insulator transition. *Phys. Rev. B* **78**, 155107 (2008).
- Eom, C. B. et al. Single-crystal epitaxial thin films of the isotropic metallic oxides Sr_{1-x}Ca_xRuO₃ (0 ≤ x ≤ 1). *Science* **258**, 1766–1769 (1992).
- Rao, R. A. et al. Strain stabilized metal–insulator transition in epitaxial thin films of metallic oxide CaRuO₃. *Appl. Phys. Lett.* **70**, 3035 (1998).
- Hyun, S. et al. Coexistence of metallic and insulating phases in epitaxial CaRuO₃ thin films observed by scanning microwave microscopy. *Appl. Phys. Lett.* **80**, 1574 (2002).
- Xia, J., Siemons, W., Koster, G., Beasley, M. R. & Kapitulnik, A. Critical thickness for itinerant ferromagnetism in ultrathin films of SrRuO₃. *Phys. Rev. B* **79**, 140407 (2009).
- Chang, Y. J. et al. Fundamental thickness limit of itinerant ferromagnetic SrRuO₃ thin films. *Phys. Rev. Lett.* **103**, 057201 (2009).
- Zayak, A. T., Huang, X., Neaton, J. B. & Rabe, K. M. Manipulating magnetic properties of SrRuO₃ and CaRuO₃ with epitaxial and uniaxial strain. *Phys. Rev. B* **77**, 214410 (2008).
- Tripathi, S. et al. Ferromagnetic CaRuO₃. *Sci. Rep.* **4**, 3877 (2015).
- He, T. & Cava, R. J. Disorder-induced ferromagnetism in CaRuO₃. *Phys. Rev. B* **63**, 172403 (2001).
- Maignan, A., Raveau, B., Hardy, V., Barrier, N. & Retoux, R. Ferromagnetism induced by chromium substitution in the CaRuO₃ perovskite. *Phys. Rev. B* **74**, 024410 (2006).
- Durairaj, V. et al. Highly anisotropic magnetism in Cr-doped perovskite ruthenates. *Phys. Rev. B* **73**, 214414 (2006).
- He, T. & Cava, R. J. The effect of Ru-site dopants on the magnetic properties of CaRuO₃. *J. Phys. Condens. Matter* **13**, 8347 (2001).
- Hardy, V., Raveau, B., Retoux, R., Barrier, N. & Maignan, A. Nature of the ferromagnetism induced by nonmagnetic substitutions on the Ru site of CaRuO₃. *Phys. Rev. B* **73**, 094418 (2006).
- Shen, S. et al. Emergent ferromagnetism with Fermi-liquid behavior in proton intercalated CaRuO₃. *Phys. Rev. X* **11**, 021018 (2021).
- Moon, E. J. et al. Structural ‘δ doping’ to control local magnetization in iso-valent oxide heterostructures. *Phys. Rev. Lett.* **119**, 197204 (2017).
- Zhang, J. Y., Hwang, J., Raghavan, S. & Stemmer, S. Symmetry lowering in extreme-electron-density perovskite quantum wells. *Phys. Rev. Lett.* **110**, 256401 (2013).
- Siwakoti, P. et al. Abrupt orthorhombic relaxation in compressively strained ultrathin SrRuO₃ films. *Phys. Rev. Mater.* **5**, 114409 (2021).
- Gao, R. et al. Interfacial octahedral rotation mismatch control of the symmetry and properties of SrRuO₃. *ACS Appl. Mater. Interfaces* **8**, 14871–14878 (2016).
- Moon, E. J. et al. Spatial control of functional properties via octahedral modulations in complex oxide superlattices. *Nat. Commun.* **5**, 5710 (2014).
- Biswas, A., Kim, K.-S. & Jeong, Y. H. Metal insulator transitions in perovskite SrRuO₃ thin films. *J. Appl. Phys.* **116**, 213704 (2014).
- Scherwitzl, R. et al. Metal-insulator transition in ultrathin LaNiO₃ films. *Phys. Rev. Lett.* **106**, 246403 (2011).
- Wang, G. et al. Role of disorder and correlations in the metal-insulator transition in ultrathin SrVO₃ films. *Phys. Rev. B* **100**, 155114 (2019).
- Shen, X. et al. Thickness-dependent metal-insulator transition in epitaxial SrRuO₃ ultrathin films. *J. Appl. Phys.* **117**, 015307 (2015).
- Ali, Z., Basaula, D., Eid, K. F. & Khan, M. Anisotropic properties of oblique angle deposited permalloy thin films. *Thin Solid Films* **735**, 138899 (2021).
- Shklovskii, B. I. & Efros, A. L. *Electronic Properties of Doped Semiconductors* Vol. 45 (Springer, 1984).
- Anderson, P. W. Absence of diffusion in certain random lattices. *Phys. Rev.* **109**, 1492 (1958).
- Ying, T. et al. Anderson localization of electrons in single crystals: Li_xFe₂Se₈. *Sci. Adv.* **2**, e150123 (2016).
- Volker, H., Jost, P. & Wuttig, M. Low-temperature transport in crystalline Ge₁Sb₂Te₄. *Adv. Funct. Mater.* **25**, 6390–6398 (2015).
- Efros, A. L. & Shklovskii, B. I. Coulomb gap and low temperature conductivity of disordered systems. *J. Phys. C Solid State Phys.* **8**, L49 (1975).
- Lien, N. V. & Rosenbaum, R. General crossovers from two-dimensional Mott T^{-1/3} to soft-gap T^{-ν} variable-range hopping. *Phys. Rev. B* **56**, 14960–14963 (1997).
- Lu, C. et al. Crossover of conduction mechanism in Sr₂IrO₄ epitaxial thin films. *Appl. Phys. Lett.* **105**, 082407 (2014).
- Mukuda, H. et al. Spin fluctuations in the ruthenium oxides RuO₂, SrRuO₃, CaRuO₃, and Sr₂RuO₄ probed by Ru NMR. *Phys. Rev. B* **60**, 12279–12285 (1999).
- Yoshimura, K. et al. ¹⁷O NMR observation of universal behavior of ferromagnetic spin fluctuations in the itinerant magnetic system Sr_{1-x}Ca_xRuO₃. *Phys. Rev. Lett.* **83**, 4397–4400 (1999).
- Lee, P. A. & Ramakrishnan, T. V. Disordered electronic systems. *Rev. Mod. Phys.* **57**, 287–337 (1985).
- Bergmann, G. Weak localization in thin films: A time-of-flight experiment with conduction electrons. *Phys. Rep.* **107**, 1–58 (1984).
- Lee, P. A. & Ramakrishnan, T. V. Magnetoresistance of weakly disordered electrons. *Phys. Rev. B* **26**, 4009 (1982).
- Kacedon, D. B., Rao, R. A. & Eom, C. B. Magnetoresistance of epitaxial thin films of ferromagnetic metallic oxide SrRuO₃ with different domain structures. *Appl. Phys. Lett.* **71**, 1724–1726 (1997).

59. Xiao, J. Q., Jiang, J. S. & Chien, C. L. Giant magnetoresistance in nonmultilayer magnetic systems. *Phys. Rev. Lett.* **68**, 3749–3752 (1992).
60. Ali, Z. et al. Controlling the charge transport mode in permalloy films using oblique angle deposition. *J. Magn. Magn. Mater.* **484**, 430–436 (2019).
61. Wu, J. et al. Intergranular giant magnetoresistance in a spontaneously phase separated perovskite oxide. *Phys. Rev. Lett.* **94**, 037201 (2005).
62. Dang, H. T., Mravlje, J., Georges, A. & Millis, A. J. Electronic correlations, magnetism, and Hund's rule coupling in the ruthenium perovskites SrRuO₃ and CaRuO₃. *Phys. Rev. B - Condens. Matter Mater. Phys.* **91**, 1–14 (2015).
63. Ishigami, K. et al. Thickness-dependent magnetic properties and strain-induced orbital magnetic moment in SrRuO₃ thin films. *Phys. Rev. B* **92**, 3–7 (2015).
64. Salamon, M. B., Lin, P. & Chun, S. H. Colossal magnetoresistance is a Griffiths singularity. *Phys. Rev. Lett.* **88**, 197203 (2002).
65. Tong, P. et al. Griffiths phase and thermomagnetic irreversibility behavior in slightly electron-doped manganites Sm_{1-x}Ca_xMnO₃ (0.80 ≤ x ≤ 0.92). *Phys. Rev. B* **77**, 184432 (2008).
66. Deisenhofer, J. et al. Observation of a Griffiths phase in paramagnetic La_{1-x}Sr_xMnO₃. *Phys. Rev. Lett.* **95**, 2–5 (2005).
67. Pramanik, A. K. & Banerjee, A. Griffiths phase and its evolution with Mn-site disorder in the half-doped manganite Pr_{0.5}Sr_{0.5}Mn_{1-y}Ga_yO₃ (y = 0.0, 0.025, and 0.05). *Phys. Rev. B* **81**, 1–5 (2010).
68. Sass, P. M. et al. Magnetic imaging of domain walls in the antiferromagnetic topological insulator MnBi₂Te₄. *Nano Lett.* **20**, 2609–2614 (2020).
69. Kresse, G. & Furthmüller, J. Efficient iterative schemes for ab initio total-energy calculations using a plane-wave basis set. *Phys. Rev. B* **54**, 11169–11186 (1996).
70. Blöchl, P. E. Projector augmented-wave method. *Phys. Rev. B* **50**, 17953–17979 (1994).
71. Joubert, D. From ultrasoft pseudopotentials to the projector augmented-wave method. *Phys. Rev. B* **59**, 1758–1775 (1999).
72. Perdew, J. P., Burke, K. & Ernzerhof, M. Generalized gradient approximation made simple. *Phys. Rev. Lett.* **77**, 3865–3868 (1996).
73. Dudarev, S. & Botton, G. Electron-energy-loss spectra and the structural stability of nickel oxide: An LSDA+U study. *Phys. Rev. B* **57**, 1505–1509 (1998).

ACKNOWLEDGEMENTS

This work is primarily supported by the US Department of Energy (DOE) under Grant No. DOE DE-SC0002136. The electron microscopic work done at Brookhaven National Laboratory (BNL) was sponsored by the US DOE-BES, Materials Sciences and Engineering Division, under Contract No. DE-SC0012704. The use of BNL Center for Functional Nanomaterials supported by BES Office of User Science Facilities for TEM sample preparation is also acknowledged. Work at Vanderbilt was supported by the U.S. Department of Energy, Office of Science, Division of Materials Science and Engineering under Grant No. DE-FG02-09ER46554 and by the McMinn Endowment at Vanderbilt University. Calculations were performed at the National Energy Research Scientific Computing Center, a DOE Office of Science User Facility supported by the Office of Science of the U.S. Department of Energy under Contract No. DE-AC02-

05CH11231. The MFM study at Rutgers is supported by the Office of Basic Energy Sciences, Division of Materials Sciences and Engineering, US Department of Energy under Award numbers DESC0018153.

AUTHOR CONTRIBUTIONS

Z.A., M.S., and J.Z. designed the research. Z.A. and M.S. grew the samples and performed the XRD, transport, and magnetization experiments. Z.W. and Y.Z. performed the STEM experiments. W.G., Y.-T.C., and W.W. performed the MFM and Hall effect experiments. A.O., D.S., and S.P. performed the calculations. All the authors contributed to the data analysis and paper writing.

COMPETING INTERESTS

The authors declare no competing interests.

ADDITIONAL INFORMATION

Supplementary information The online version contains supplementary material available at <https://doi.org/10.1038/s41535-022-00518-7>.

Correspondence and requests for materials should be addressed to Yimei Zhu, Sokrates T. Pantelides or Jiandi Zhang.

Reprints and permission information is available at <http://www.nature.com/reprints>

Publisher's note Springer Nature remains neutral with regard to jurisdictional claims in published maps and institutional affiliations.



Open Access This article is licensed under a Creative Commons Attribution 4.0 International License, which permits use, sharing, adaptation, distribution and reproduction in any medium or format, as long as you give appropriate credit to the original author(s) and the source, provide a link to the Creative Commons license, and indicate if changes were made. The images or other third party material in this article are included in the article's Creative Commons license, unless indicated otherwise in a credit line to the material. If material is not included in the article's Creative Commons license and your intended use is not permitted by statutory regulation or exceeds the permitted use, you will need to obtain permission directly from the copyright holder. To view a copy of this license, visit <http://creativecommons.org/licenses/by/4.0/>.

© The Author(s) 2022